



Co-funded by the European Union

Project No : 101094628

Project Number:
101094628

Project Acronym:
ESSnuSBplus

Call Identifier:
HORIZON-INFRA-2022-DEV-01

Project Full Title:
Study of the use of the ESS facility to accurately measure the neutrino cross-sections for ESSnuSB leptonic CP violation measurements and to perform sterile neutrino searches and astroparticle physics

Start date of project: 2023-01-01
Duration: 4 years
Deliverable title: Design of the Target Station
Due delivery date: 2026-10-31
Actual delivery date: 2026-10-31
Organisation name of lead contractor for this milestone: Centre National de la Recherche Scientifique (CNRS)

Project co-funded by the European Commission within Horizon Europe Framework Programme		
Dissemination level		
PU	Public	X
CO	Confidential, only for members of the consortium (including the Commission Services)	
EU-RES	Classified information: RESTREINT UE (Commission Decision 2005/444/EC)	
EU-CON	Classified information: CONFIDENTIEL UE (Commission Decision 2005/444/EC)	
EU-SEC	Classified information: SECRET UE (Commission Decision 2005/444/EC)	

Deliverable number	D3.3
Deliverable name	Design of the Target Station
Type of document	Report
Work Package	WP3: Target Station & Pion Extraction
Lead Contractor	CNRS, France
Lead Institutes	UHH, CERN, CNRS

Authors' name	Organisation	Email
Jorge Aguilar	ESSB	jaguilar@essbilbao.org
Eric Baussan	CNRS	eric.baussan@iphc.cnrs.fr
Elian Bouquerel	CNRS	elian.bouquerel@iphc.cnrs.fr
Ting W. Choi	Uppsala University	ting.choi@physics.uu.se
Ilias Efthymiopoulos	CERN	Ilias.Efthymiopoulos@cern.ch
Caren Hagner	UHH	caren.hagner@desy.de
Julien Hiegel	CNRS	julien.hiegel@iphc.cnrs.fr
Maria López Reguera	ESSB	mlopez@essbilbao.org
Miguel Magán	ESSB	mmagan@essbilbao.org
Maja Olvegård	Uppsala University	maja.olvegard@physics.uu.se
Pascal Poussot	CNRS	pascal.poussot@iphc.cnrs.fr
Cedric Schwab	CNRS	cedric.schwab@iphc.cnrs.fr
Fernando Sordo Baldin	ESSB	fsordo@essbilbao.org
Tamer Tolba	UHH	tamer.tolba@uni-hamburg.de
Max Topp-Mugglestone	CERN	max.emil.topp-mugglestone@cern.ch
Jacques Wurtz	CNRS	jacques.wurtz@iphc.cnrs.fr
Valeria Zeter	CNRS	valeria.zeter@iphc.cnrs.fr

Abstract

The target station facility is key element of the European Spallation Source neutrino Super-Beam (ESSνSB)+ project which will allow to provide a neutrino beam to perform cross section measurement and sterile neutrino study. The production of the neutrino superbeam comes from the decay in flight of muons stored in a racetrack ring. This ring is filled with pions produced by the target station. This deliverable presents the proposed design of the overall elements of the target station facility. In particular, the hadronic collector with its element such the granular target, the magnetic horn, the large aperture dipole and the target to ring transfer line will be presented.

List of abbreviations and acronyms

Abbreviation	Description
BEW	Beam Entrance Windows
CLMT	Collimator
DSS	Downstream shielding structure
ESS	European Spallation Source
ESSnuSB	European Spallation Source neutrino Super-Beam
LADM	Large-Aperture Dipole Magnet
LEnuSTORM	Low Energy neutrinos from STOred Muons
LBL	Long BaseLine
nuSTORM	neutrinos from STOred Muons
T2R	Target to Ring
WP	Work Package

Contents

1 Overview **5**

2 Target Station **5**
2.1 Magnetic Horn 6
2.2 Granular Target 9
2.2.1 Baseline cooling and structural concept 9
2.2.2 Realistic packing and porous-medium coefficients 10
2.2.3 ETTF experimental validation 11
2.3 Target Integration 13
2.3.1 Cooling concepts and assessment method 13
2.3.2 Structural results 14
2.3.3 Pressure cost and available radial space 15

3 The Power Supply of the hadronic collector based on one magnetic horn. **16**
3.1 Principle of Pulse Generation 17
3.1.1 Modularity approach of the PSU. 18
3.1.2 The 44kA output unit 19
3.2 Mechanical implantation 19

4 The focusing and the pion extraction systems . **21**

5 Target Station Facility **22**
5.1 Power deposition and shielding 22
5.2 Dose deposition at the dipole level 25

6 Conclusion **26**

1 Overview

The European Spallation Source (ESS) facility dedicated to neutron production offers an unique opportunity to produce a high intensity neutrino beam in Europe to study fundamental properties of neutrinos. An upgrade of the facility, the ESSνSB was proposed to produce such a beam based on the 5 MW proton beam power [1] with 2.5 GeV energy. Following the time schedule implementation of the ESS linac, an intermediate facility ESSνSB+ has been proposed working at 1.25 MW and will be able to perform additional measurement such neutrino cross section measurement and to study sterile neutrino. A staging approach has been proposed taking in account its power increase:

- A monitored beam working a low energy at about 3 kW (Phase 1)
- A superbeam working at an intermediate beam power 1.25 MW (Phase 2)
- A superbeam working at full beam power 5 MW (Phase 3)

In the phase 3, the neutrino beam is produced by a target station facility converting the 5 MW proton beam into pions thanks to an hadronic collector composed of four magnetic horns able to work at 1.25 MW each and a 50 m long decay tunnel to let the pions to decay into neutrinos. In Phase 2, the neutrino beam will be produced by the decay in flight of muon particles stored in a racetrack ring. In thjis case, the target station facility will use only one horn at 1.25 MW and feed in pions the low energy race track ring. The building requires a certain number of new elements to guide the pions to the racetrack ring, such a Large-Aperture Dipole Magnet (LADM) and a Target to Ring (T2R) line equipped with quadrupole magnets. In this deliverable, the design of the elements of the target station facility will be presented.

2 Target Station

The target station of the ESSνSB+ project consists of only one magnetic horn equipped with a granular target made of titanium spheres as shown in Figure 1.

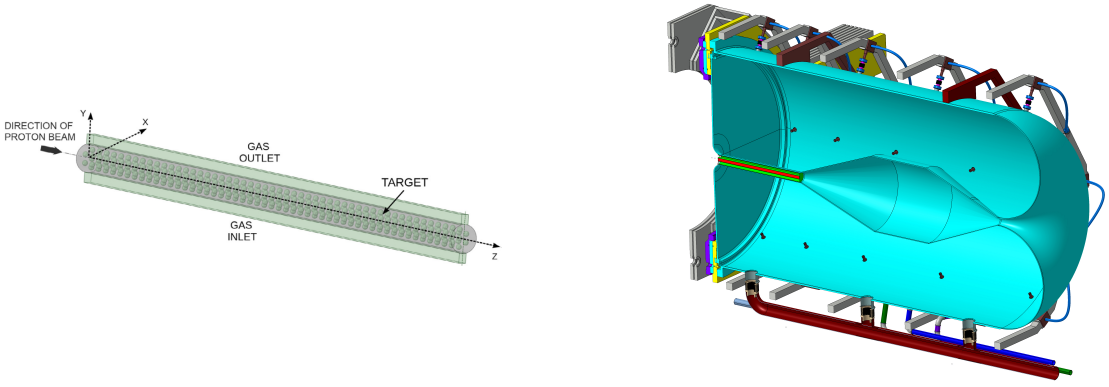


Figure 1: Granular Target Concept (Left) Magnetic Horn (Right)

The ESSνSB hadronic collector has been designed to optimise the δ_{CP} sensitivity, taking into account the neutrino beam flux and the response of the Water Cherenkov detector. In the case of the present project, the horn has been re-optimised to maximize the pions flux in the T2R line in the energy range required to reach the physics goals.

of with respect to the physics goals.

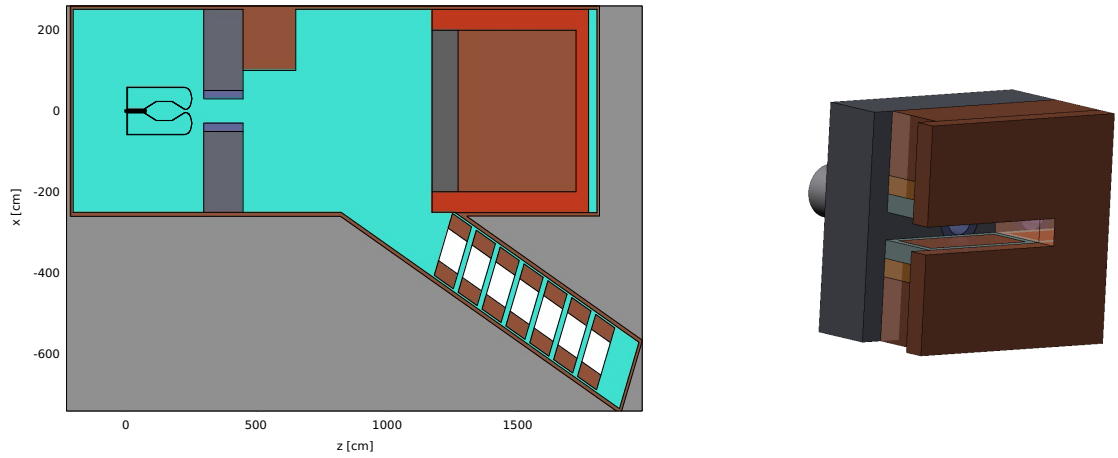


Figure 2: Simplified geometry used in the FLUKA simulation. From left to right, the target and magnetic horn are followed by the collimator and its tungsten ring, and then by the large aperture dipole, which deflects the particles towards the transfer line shown at the bottom of the figure. The transfer line contains quadrupole magnets only for illustration. The beam dump is located at the far right of the geometry.

Figure 2 represents a simplified used design for the simulation in FLUKA environment [2, 3] of the particle propagation from their production to the entrance of the T2R lines and to estimate the power deposition in the surrounding environment.

2.1 Magnetic Horn

The secondary particles produced in the target have a broad momentum and angular distribution. In particular, the produced pions are emitted over a wide range of angles with respect to the proton beam axis. A magnetic horn is therefore used to increase the acceptance of the pion beam and focus positively (or negatively) charged pions towards the beam axis. The horn generates a strong toroidal magnetic field, which modifies the transverse momentum of the charged pions and consequently reduces their angular divergence downstream of the collimator.

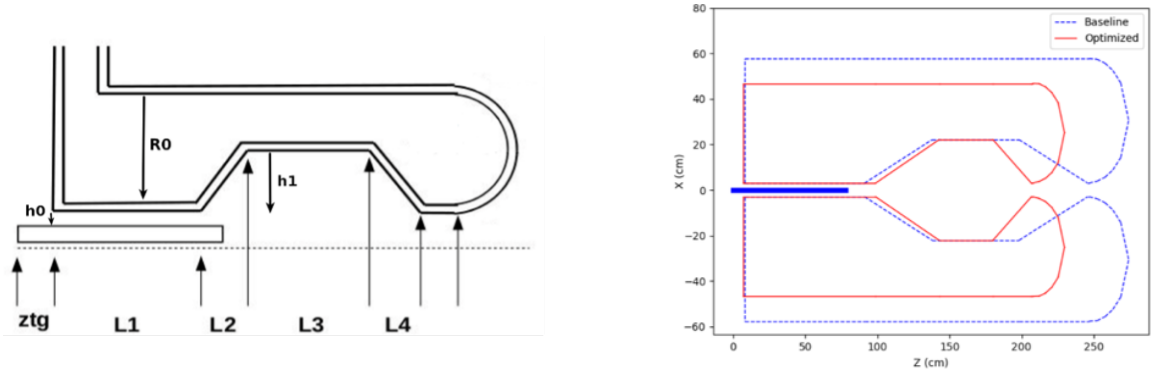


Figure 3: Horn scheme used for the optimisation with the the parameters defining the inner conductor (Left) Result of the optimisation (Right)

The result of the process of horn optimisation is illustrated in Figure 3 and the results given in Table 1. A Genetic Algorithm (GA) was used to optimise the main horn geometry parameters by maximising the pion flux at the selected aperture. The optimized configuration reported in Table 1, results in an overall reduction of the horn dimensions compared with the baseline from the ESSνSB geometry.

Table 1: Optimized horn geometry values obtained from the genetic algorithm (GA). The parameters L_5, h_0, and h_1 are kept constant.

Parameter	Baseline [cm]	Scale factor range	Best fit [cm]
L_1	83.08	[1.0, 2.5]	91.66
L_2	46.80	[0.5, 2.5]	43.99
L_3	60.30	[0.5, 2.5]	37.38
L_4	47.50	[0.5, 2.5]	26.60
L_5	1.08	–	1.08
R_0	54.40	[0.5, 2.5]	43.52
h_0	3.30	–	3.30
h_1	22.10	–	22.10
z_{tg}	8.10	[0.5, 2.5]	7.14

The pion distributions were investigated at the target level, representing the pions production, downstream of the target, after the magnetic horn at several locations.

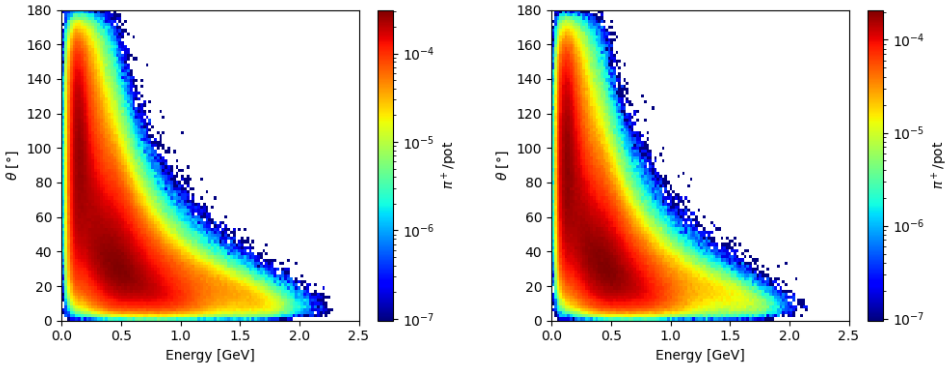


Figure 4: Angle of the π^+ (left) and π^- (right) as a function of their energy at the target level.

Figure 4 shows the phase space distribution of the pions in the angle-energy phase space. The distributions of positive and negative pions are relatively similar, although fewer negative pions are produced. In addition, the pions exhibit a wide angular spread with respect to the beam axis, highlighting the need for a magnetic horn to focus the secondary particles.

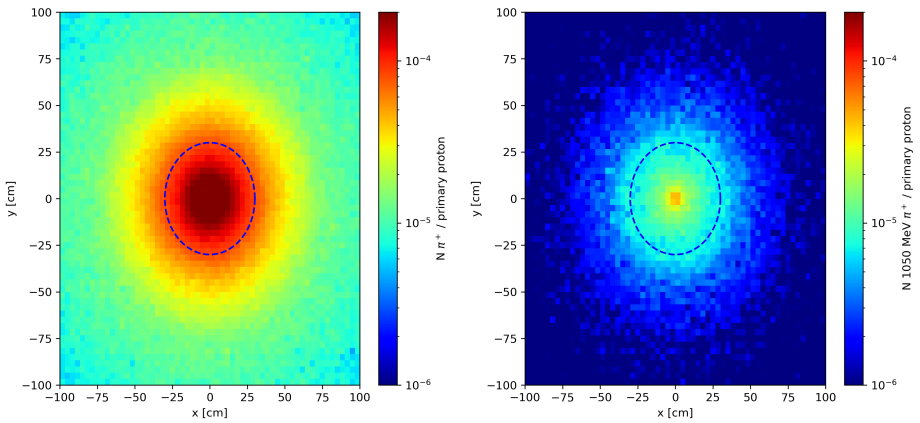


Figure 5: Full distribution of π^+ (Left) and with 1050 MeV (Right) at 56 cm after the horn's end (z = 300 cm at the collimator position). The blue circle represents the aperture of the collimator.

Figure 5 shows the transverse spatial distribution of the produced π^+ at $z = 300$ cm, corresponding to the entrance plane of the collimator. The left figure shows the distribution of π^+ over the full energy range, while the right figure shows only pions with an energy of 1050 MeV. In both cases, the pion distribution is centred around the beam axis, showing the expected focusing effect of the magnetic horn. The 1050 MeV pions are less numerous, as expected, but remain well centred around the beam axis, indicating that they are efficiently transported through the horn towards the downstream system.

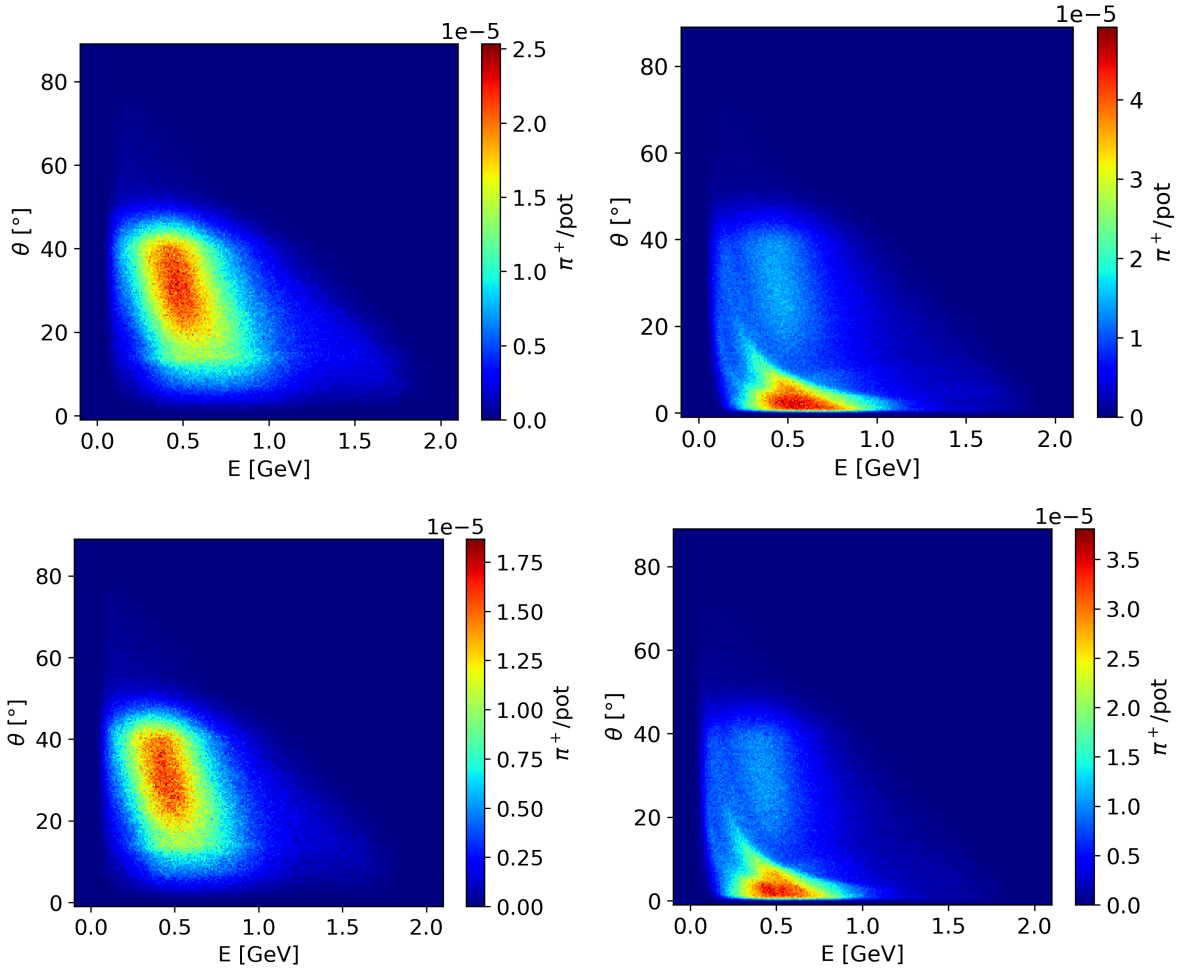


Figure 6: Pion angle as a function of energy at the CLMT level. The top panels show positive pions, while the bottom panels show negative pions. No focusing is applied in the left panels, whereas the right panels show the corresponding distributions after magnetic horn focusing.

Figure 6 shows the pion distribution at the CLMT level in the angle-energy phase space. The left panels correspond to the configuration without magnetic horn focusing, while the right panels show the distributions after the corresponding focusing of positive and negative pions. Without focusing, the pions retain a relatively broad angular distribution, with a significant fraction of particles emitted at large angles with respect to the beam axis. After passing through the magnetic horn, the angular spread is significantly reduced, demonstrating the focusing effect of the horn. The pions are concentrated towards smaller angles, while the overall energy distribution remains broadly similar. This confirms that the magnetic horn efficiently redirects the secondary pions towards the beam axis, increasing the fraction of particles that can be transported through the downstream collimator and transfer line.

2.2 Granular Target

A granular target has been developed from an initial helium-cooled concept to a design supported by progressively higher-fidelity thermal–hydraulic, mechanical and experimental evidence. The development was deliberately staged: the 2023 work established a workable target and beam Beam Entrance Windows (BEW) cooling arrangement; the 2024–2025 work addressed the response of individual spheres and the fidelity of the porous-medium model; and the 2026 campaign commissioned the Experimental Target Test Facility (ETTF) and acquired the first hydraulic and thermal histories from a representative granular assembly. The principal achievements and the remaining limitations are reported below.

2.2.1 Baseline cooling and structural concept

The baseline target is a cylindrical canister filled with 3 mm titanium-alloy spheres and cooled by pressurised helium. A dedicated bypass through the BEW was introduced to prevent an excessive pressure loss across the porous region while maintaining direct cooling of the window. For the nominal 0.2 kg s^{-1} flow, approximately 0.18 kg s^{-1} crosses the sphere bed and 0.02 kg s^{-1} crosses the BEW. The corresponding calculated pressure loss with the bypass is about 0.7 bar, besides the porous-zone and BEW peak temperatures were approximately 370 °C and 530 °C, respectively [4].

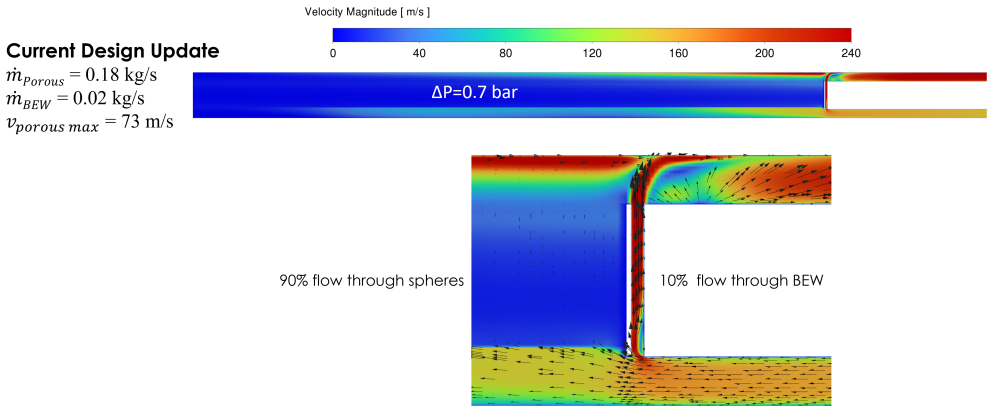


Figure 7: BEW bypass concept and calculated helium-flow split. The bypass provides direct window cooling and reduces the total pressure loss.

The associated static structural assessment showed a maximum equivalent Von Mises stress of 188 MPa for pressure loads. The results for pressure and temperature loads yield a maximum stress of 300 MPa. Table 2 shows the comparison values with the applicable normative, and shall be conclude that the proposed design satisfies the requirements.



(a) Pressure Loads

(b) Pressure + Temperature Loads

Figure 8: Linearisation Stress Calculation.

Table 2: Stress assessment according to RCC-MRx.

		Stress [MPa]	Model Ti Alloy Ti-6Al-2Sn-4Zr-2Mo	Titanium Alloy Ti-6Al-4V
Primary stresses				
Membrane stress	$P_m \leq S_m$	8.9	337	390
Membrane + Bending stress	$P_m + P_b \leq 1.5S_m$	96.7	505	585
Primary + Secondary stresses				
Membrane stress	$P_m + Q_m \leq S_m$	298.5	337	390
Membrane + Bending stress	$P_m + Q_m + P_b + Q_b \leq 1.5S_m$	300.0	505	585

2.2.2 Realistic packing and porous-medium coefficients

The initial target calculations represented the titanium spheres as a homogeneous porous medium with an assumed porosity of approximately $\varepsilon = 0.34$. However, this value corresponds to an exceptionally dense packing configuration and does not account for the geometrical constraints imposed by the canister walls. Considering the 3 mm sphere diameter and the 30 mm canister diameter, a more realistic determination of the packing arrangement was required to improve the prediction of pressure drop and heat extraction.

In 2025, a Python-based random packing algorithm, based on the Lubachevsky–Stillinger approach, was developed to generate realistic, non-overlapping sphere distributions. Three different random seeds (42, 50 and 72) were initially considered for a representative 12 mm-long section of the canister. Each configuration contained 309 spheres, corresponding to a solid fraction of 0.541 and a geometrical porosity of 0.459, significantly higher than the previously assumed value.

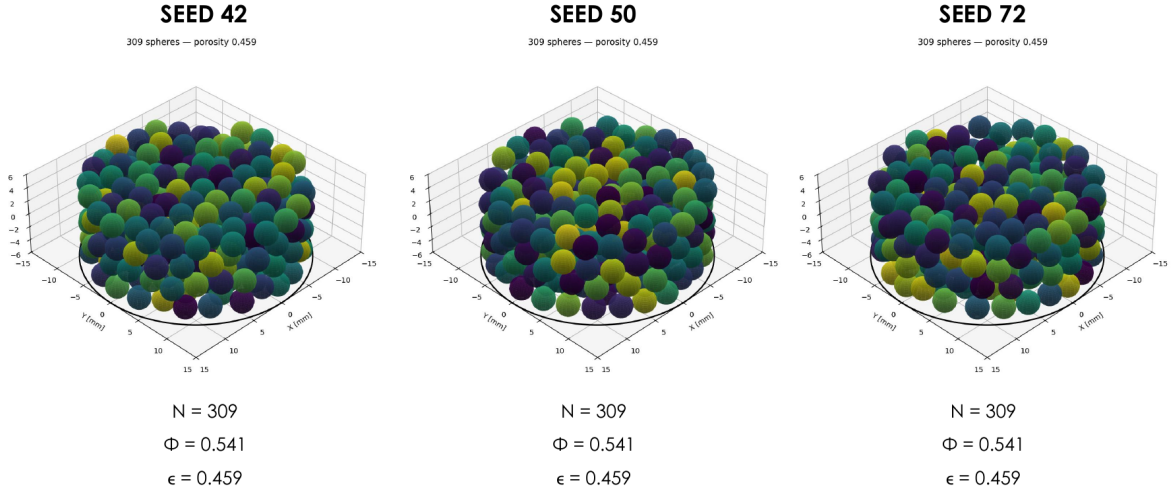


Figure 9: Random packing distributions generated using three different seeds for the 6 mm-long canister slice.

The hydraulic behavior was first estimated analytically using the Ergun correlation, which expresses the pressure drop through a packed bed as the sum of viscous and inertial contributions. Detailed CFD simulations were subsequently performed on the explicitly resolved sphere

geometries to evaluate the limitations of this approximation. Different superficial velocities were imposed, and the resulting pressure losses were fitted to the Darcy–Forchheimer formulation to obtain the corresponding viscous (C_1) and inertial (C_2) resistance coefficients.

The three random configurations produced very similar pressure-drop results, indicating a limited sensitivity to the particular sphere arrangement. However, significant differences were observed between the analytical Ergun predictions and the detailed CFD results, as summarised in Table 3.

Table 3: Comparison between Ergun-based and CFD-calibrated porous-medium resistance coefficients.

Coefficient	**Ergun correlation**	**CFD (mean $\pm$ variation)**
C_1 [m^{-2}]	5.35×10^7	$(6.29 \pm 0.15) \times 10^8$
C_2 [m^{-1}]	6.85×10^3	$(3.33 \pm 0.03) \times 10^3$

The detailed CFD predicted a viscous resistance approximately 11.8 times higher than the Ergun estimate, whereas the inertial resistance was approximately 0.49 times the analytical value. These discrepancies are attributed to the complex flow paths, local channeling and wall effects associated with the confined granular geometry. Consequently, adjusting the porosity alone cannot reproduce both resistance contributions, demonstrating the need to calibrate C_1 and C_2 independently for the reduced porous-medium model.

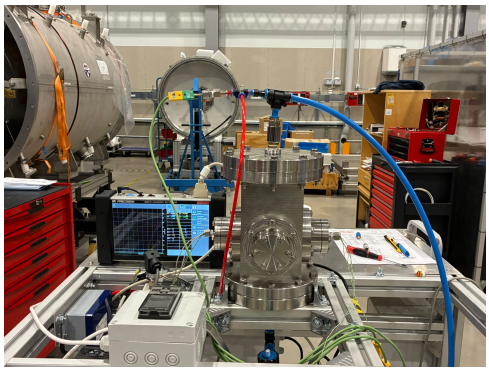
The packing analysis was subsequently extended to the complete canister, with an overall length of 77 mm. For the reference packed volume of 30×69 mm, the Python model predicted 1970 spheres, corresponding to a solid fraction of 0.577 and a porosity of 0.423.

This prediction was later verified experimentally using a 3D-printed reference cylinder filled with the actual titanium spheres. A total mass of 129.005 g was introduced, equivalent to approximately 1955 spheres considering an average mass of 66 mg per sphere. The resulting experimental porosity was approximately 0.433, showing good agreement with the numerical prediction, with an absolute difference of only 0.010. Additional vibration during filling did not lead to any appreciable improvement in the packing density.

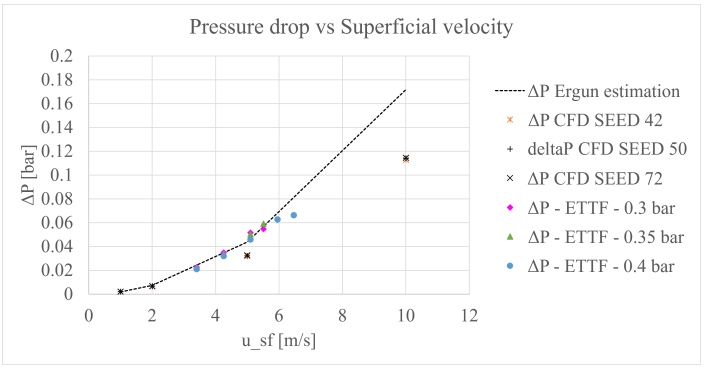
Overall, the study demonstrated that the original porosity assumption significantly underestimated the void fraction of the granular target.

2.2.3 ETTF experimental validation

The ETTF programme converted the main modelling uncertainties into measurable quantities. The preliminary facility concept defined in 2024 was developed into detailed geometry and drawings in 2025, followed by assembly and operation at MML–ESS in Lund in 2026. The completed rig includes the granular canister, a controlled air circuit, a heater, pressure instrumentation, multiple thermocouples and multichannel acquisition. The test procedure consisted on two parts, on the one hand, it was required to obtain ~ 10 quasi-steady operating points at different operating pressure set-points and increasing from low flow up to the maximum achievable flow. On the other hand, a second procedure was performed at a fixed operating pressure both for a low-flow and high-flow points in order to measure heating and cooling times following [5].



(a) Assembled ETTF rig and acquisition hardware.



(b) Pressure drop as a function of Superficial velocity.

Figure 10: Experimental evidence produced during the 2026 ETTF campaign.

The experimental results indicate that the **inertial contribution** is the dominant term of the Darcy–Forchheimer/Ergun pressure-drop relationship within the range reported. In the present experiments, the measured pressure drop shows a clear *non-linear dependence* on superficial velocity, indicating that the quadratic contribution has a greater influence than the linear one. This is also reflected in the fitted coefficients: C_2 is obtained with relatively moderate uncertainty, whereas C_1 presents a much larger uncertainty and is therefore poorly constrained by the available experimental data.

$$\frac{\Delta P}{L} = \underbrace{150\frac{\mu(1-\varepsilon)^2}{\varepsilon^3 d_p^2}\, u_{sf}}_{\text{Viscous term}} + \underbrace{1.75\frac{\rho(1-\varepsilon)}{\varepsilon^3 d_p}\, u_{sf}^2}_{\text{Inertial term}}$$

This behaviour is consistent with both the Ergun estimation and the CFD calculations. The Ergun correlation predicts an increasing contribution of the quadratic term as the superficial velocity and particle Reynolds number increase, and the CFD results show the same non-linear evolution of pressure drop with velocity. The experimental measurements reproduce this same trend and therefore support the overall behaviour predicted by the analytical and numerical approaches.

For one of the operating pressures, the fitted value of C_1 becomes negative. This value should not be interpreted as a physically negative viscous resistance. Instead, it indicates that *the linear contribution is too small relative to the quadratic contribution* to be determined independently with sufficient accuracy over the available velocity range. Since the linear and quadratic fitting coefficients are strongly coupled, small changes in the experimental data or in the fitted quadratic coefficient can cause the linear coefficient to change significantly and even become negative while producing almost the same overall pressure-drop curve. Therefore, the negative C_1 value is an indication of poor identifiability of the viscous term rather than a physical effect.

Table 4: Comparison between Ergun-based, CFD-calibrated and ETTF-experimental porous-medium resistance coefficients.

Coefficient	**Ergun correlation**	**CFD (mean $\pm$ variation)**	**ETTF**
			(0.3 bar)
C_1 [m^{-2}]	5.35×10^7	$(6.29 \pm 0.15) \times 10^8$	$(1.29 \pm 1.57) \times 10^8$
C_2 [m^{-1}]	6.85×10^3	$(3.33 \pm 0.03) \times 10^3$	$(7.76 \pm 0.78) \times 10^3$
			(0.35 bar)
			$(-9.19 \pm 3.19) \times 10^8$
			$(8.31 \pm 0.16) \times 10^3$
			(0.4 bar)
			$(1.84 \pm 1.57) \times 10^8$
			$(6.01 \pm 0.63) \times 10^3$

Heating and cooling rates were recorded at several heater set points, including approximately 250 °C and 400 °C. Cooling runs near 1.1 g s^{-1} and 3.7 g s^{-1} showed the expected faster response at higher flow, confirming that the selected method is sensitive to the heat-transfer regime.

Before the experimental campaign, the design relied on analytical Ergun estimates and CFD predictions. The campaign now provides measured pressure and temperature information to calibrate C_1 and C_2, quantify uncertainty and compare the resolved and porous CFD models under relevant operating conditions.

2.3 Target Integration

The main challenge in target–horn integration is target bending, driven primarily by the temperature difference between opposite sides of the titanium structure and the resulting differential thermal expansion. The present concept retains an upstream support and a free downstream end, simplifying insertion and replacement. The horn inner radius is 40 mm (80 mm diameter), whereas the current target outer radius is 29 mm. The nominal radial allowance is therefore only 11 mm, to accommodate deformation, any additional cooling sleeve and the required operating clearance.

2.3.1 Cooling concepts and assessment method

Two mitigation strategies have been investigated to reduce the temperature difference across the target and the resulting bending:

- **Internal helium bypass:** slots in the lateral ribs divert cold helium towards the hot collector, forming a cooling film along the upper wall.
- **External circumferential cooling:** a uniform heat transfer coefficient is applied to the outer cylindrical wall to assess the potential benefit of an additional annular helium channel.

The first mitigation introduces **slots in the lateral ribs** connecting the cold and hot collectors. The bypass forms a colder helium film along the upper wall, shielding it from hot helium leaving the beam entrance window and granular bed. Three longitudinal positions were investigated (Figure 11). The intermediate arrangement gave the best thermal compromise in that

screening: upstream diversion reduced flow available to the bed, while downstream injection provided insufficient protection of the hottest shell region [6, 7]. The supplied temperature field used here corresponds to the intermediate position.

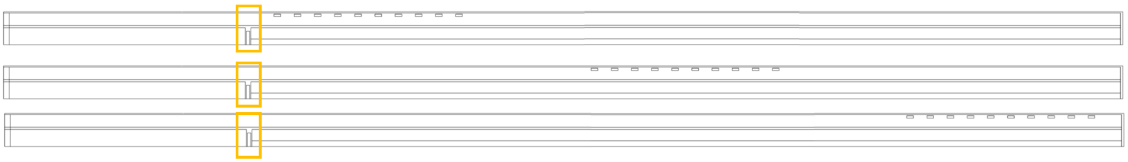


Figure 11: Upstream, intermediate and downstream slot positions, from top to bottom. The highlighted beam window provides a common reference. Adapted from [6].

The second approach applies **uniform external convection** around the cylindrical wall: five CFD cases used $h = 1800$–$5500\,\mathrm{W\,m^{-2}\,K^{-1}}$ and a fixed 20 °C sink. The annulus itself was not modelled. The HTC sweep and supplied slot case retained the same total helium flow of $0.20\,\mathrm{kg\,s^{-1}}$, inlet temperature and deposited power.

2.3.2 Structural results

The temperature fields were transferred to the existing structural model, with temperature applied after gravity and pressure loading. The assessment retains a rigid upstream support and small-deflection behaviour; neither slot-induced stiffness changes nor an added sleeve are represented. Block C was read from its latest saved structural solution, retaining its original no-slot thermal field [8].

The reference solution (no bending mitigation strategy) gives a maximum transverse tip movement of 12.03 mm. The intermediate-slot field reduces this to 7.12 mm, while the external-HTC cases give 7.39 mm to 5.11 mm (Table 5). Relative to the reference, these are approximately 41% and 39–58% reductions, respectively, in this preliminary comparison. Within the HTC sweep, the maximum outer-wall temperature decreases from 194.8 °C to 113.8 °C, and the mean upper–lower wall temperature difference from 61.2 K to 30.2 K. Figure 12 shows the axial thermal and displacement profiles, including the reference case.

Table 5: Structural results and separate annular-channel estimates. Pressure columns are the *additional annular loss*, excluding the existing target circuit. b is an illustrative residual radial budget, not a computed minimum clearance.

Case	h [W m^{-2} K^{-1}]	Tip $\lvert u_Y \rvert$ [mm]	g [mm]	$\Delta p_{K=0}$ [bar]	$\Delta p_{K=2}$ [bar]	b [mm]
Reference	0	12.03	–	0	0	−1.03
Intermediate slots	0	7.12	–	0	0	3.88
External HTC	1800	7.39	5.96	0.136	0.307	−2.35
External HTC	2500	6.65	4.30	0.379	0.725	0.05
External HTC	3500	5.95	3.07	1.075	1.779	1.98
External HTC	4500	5.46	2.39	2.332	3.521	3.15
External HTC	5500	5.11	1.96	4.316	6.120	3.94

g: equivalent radial flow gap from the analytical model below. $b = 11 - g - \lvert u_Y \rvert$ in mm, with $g = 0$ for reference and slots. It excludes sleeve thickness, other deformation components, horn expansion and tolerances. Zero annular loss does not mean zero internal target loss. Large pressure-drop estimates require compressible reassessment.

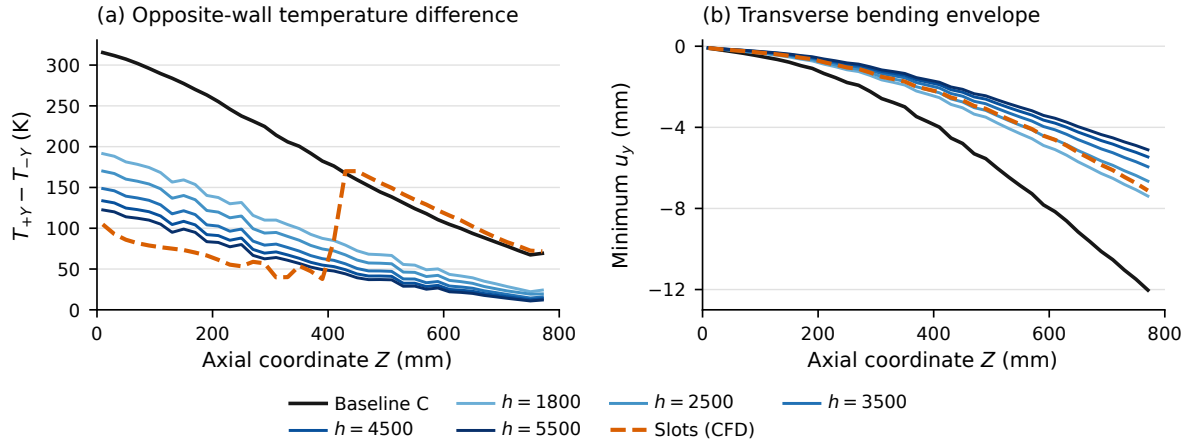


Figure 12: Reference C, intermediate slots and external-HTC cases on the retained structural mesh. (a) Temperature difference between opposite outer-wall generators at $X = 0$, $Y = \pm 29$ mm, averaged over matched node pairs in 20 mm axial bins. (b) Minimum global u_Y in each bin at the final load step. HTC values are in $\mathrm{W\,m^{-2}\,K^{-1}}$.

2.3.3 Pressure cost and available radial space

The hydraulic estimate uses a smooth, concentric, 0.983 m-long annulus outside $R = 29$ mm, carrying the full $0.20\,\mathrm{kg\,s^{-1}}$ of helium at 10 bar absolute. Reference bulk and heated inner-wall temperatures are 20 °C and 100 °C; the outer wall is treated as adiabatic. The annular Gnielinski correlation [9] gives the equivalent gaps in the table. Additional pressure loss is estimated with constant properties as

$$\Delta p_{\mathrm{ann}} = \left(f_D \frac{L}{2g} + \sum K \right) \frac{\rho v^2}{2}.$$

Here $K = 0$ includes straight-channel friction only, while $\sum K = 2$ is an illustrative allowance for local losses, not a designed collector. The five HTC CFD cases already have approximately 0.55 bar internal total-pressure loss, excluding the annulus. Thus external cooling has a substantial additional hydraulic cost. At $h \geq 3500\,\mathrm{W\,m^{-2}\,K^{-1}}$, the large pressure fractions require compressible reassessment; the highest-HTC estimate also reaches $M \simeq 0.33$.

The reference displacement alone exceeds the nominal 11 mm radial allowance by about 1.03 mm. Slots leave an illustrative 3.88 mm budget without enlarging the outer envelope. For external cooling, the gap consumes part of the recovered space: the approximately 6 mm option gives $b \simeq -2.35$ mm, and the 4.30 mm option leaves only 0.05 mm, even before sleeve thickness. Smaller gaps improve this geometric budget but sharply increase pressure loss. These budgets use the unchanged target's displacement; they are not a contact analysis of the new assembly or a validation of clearance.

The resulting design direction is to combine a smaller target envelope and/or greater structural stiffness with circumferential cooling, and then model the complete annular flow in series before the existing cold collector. Helium warming, real manifolds, sleeve deformation and the expanded horn must be included before a gap is selected. That complete model is deferred.

3 The Power Supply of the hadronic collector based on one magnetic horn.

The concept of the Power Supply Unit (PSU) inherits from the ESSνSB project in the case of a hadronic collector based on four horns [1]. The working conditions of ESSνSB+ project are based similar on most of the many aspects but require many update. In particular, only one additional H^- pulses between the proton pulses in the linac chain is necessary for Phase 2, as represented in Figure 13. After stripping of the $H-$ and time shortening into the accumulator, the remaining proton pulses hit the granular target.

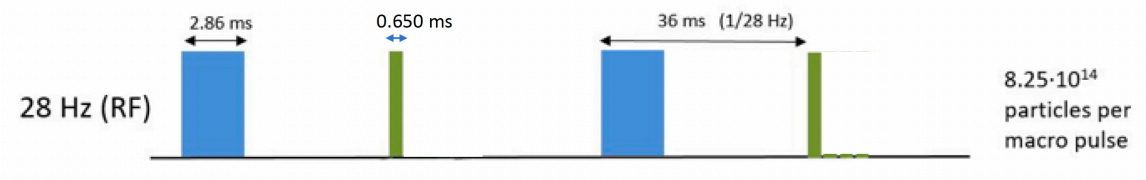


Figure 13: Proton beam baseline pulse timing structure showing both protons (ESS) and H- (ESSνSB+).

The magnetic horn will be pulsed at 14 Hz with a high intensity current pulse of 350 kA to produce the magnetic field and has be synchronised with the proton pulse coming out the accumulator as shown in Figure 14.

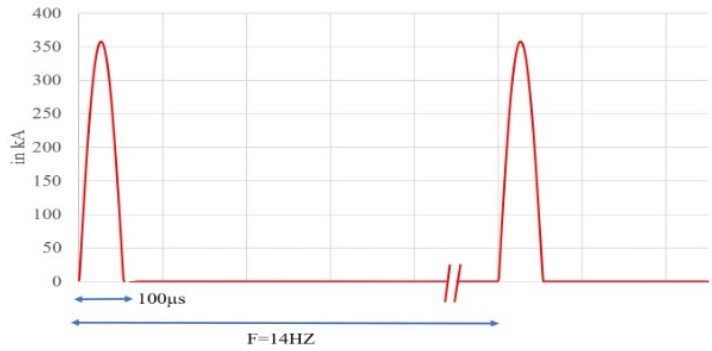


Figure 14: ESSnuSB+ Horn Pulse Current.

The electrical pulses of the PSU are synchronized with the proton beam pulses. The power supply has been studied based on the following main requirements:

- the horn is pulsed by a half sinusoid current waveform of 100μs width and 350 kA peak current with a very high RMS current of 9.3 kA at a high 14Hz frequency. The magnetic horn is a real short circuit with a very low inductance of 0.77 μH and a low resistance value of 0.211 mΩ.
- - the electrical solution proposed must reduce the thermal dissipations in the horns at their minimum and allows to recover the maximum of energy.
- the margin safety of PSU components should be dimensioned to accept very high electrical constraints and high reliability while operating with a long lifetime of 3.6Billions of cycles (300 days by year, during 10 years)
- to improve efficiency components will be water cooled (this allows also to recycle the heat).
- for raison of safety and maintainability the operating voltage is limited to 20kV.

3.1 Principle of Pulse Generation

To generate the pulse current, we'll use the principle of charging a capacitor bench C to a Vo high voltage reference and then the energy of capacitors we'll be discharged by a bigswitch directly to the horn via a design of well dimensioned 33 m length striplines (Figure **??**). A recovery stage, made by a recovery diode Dr and recovery coil Lr is used after the discharge step, reverting fastly the negative voltage of capacitor C to the Vend value. After this cycle the charger provides additional current to bring the voltage of the capacitor up to the reference high voltage Vo.

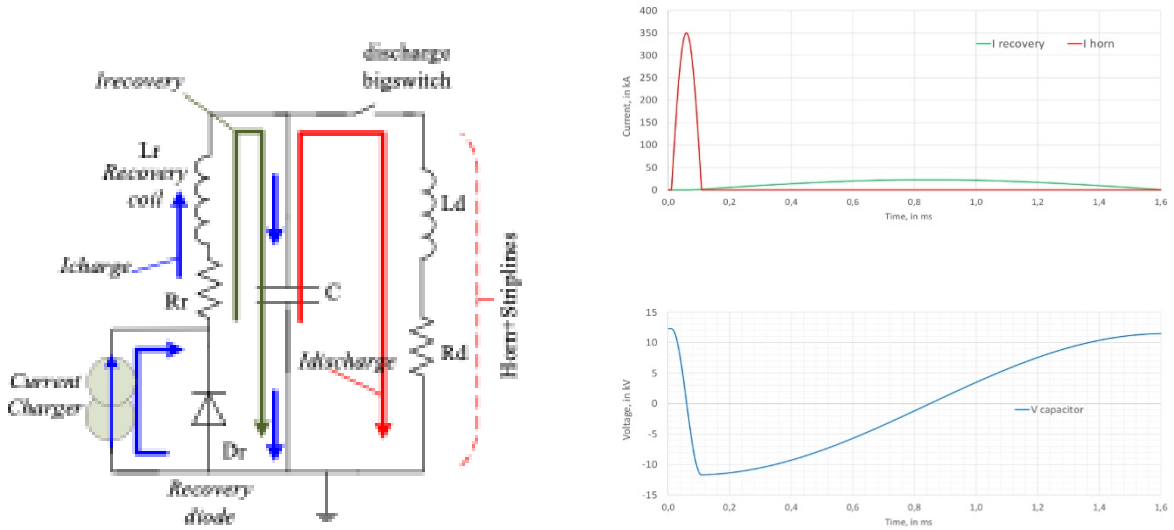


Figure 15: Principle of delivering 350 kA peak current during 100 μs half period to magnetic horn (Left) Current and voltage of a capacitor bench during discharge and recovery (Right).

The low values of resistivity in discharge and recovery circuit allow to bring high efficiency of the PSU.

Table 6: Electrical constraints of the PSU for a horn pulsed at 14 Hz.

PSU	ESSnuSB+
I peak, kA	350
C, μF	1120
+Vo/+Vend, kV	10.5/9.6
Idischarge dI/dt, kA/μs	11
Idischarge RMS, A	9300
Irecovery peak, kA	20
Irecovery RMS, A	2200

The values of critical electrical constraints in discharge and recovery stages are given in Table 6 and verified by simulation with the PSIM software [10]. The resistivity and inductance values in discharge and recovery circuits are explained later in Annexe 5.

It results very high values of peak and RMS currents in discharge and recovery circuit, so it will not be able to find any switch component or coil that could accept these high electrical constraints. Therefore, a modular approach is used to reduce the electrical constraints on various components and is explained in section 3.1.1.

To reduce at minimum the values of resistivity and inductance on the striplines, investigations have been done in the previous project [1]. The optimal solution is obtained by using 8 plates in 6061-T6 of 60 cm width, 2 cm of thickness, spaced by 1cm and mounted in parallel. The electrical characteristics of the horn and the strip lines are given in Table 7.

Table 7: Electrical characteristics of the horn and for the 33 m length of striplines.

L horn [nH]	770
R horn, [$\mu\Omega$]	213
L stripline, [nH]	441
R stripline, [$\mu\Omega$]	1676

3.1.1 Modularity approach of the PSU.

To reduce electrical constraints on components we have defined a module who deliver only 44 kA. Regardless of the high electrical constraints applied on the bigswitch and by choosing the best thyristors or diodes of manufacturers as ABB or INFINEON it is possible to have sufficient margin safety. To reduce length of striplines at minimum the components of the module will be place in height for providing small area at ground, and it will also possible to have module who deliver to outputs of 44kA. The modular solution of the total PSU is shown in Figure 16. All the capacitors benches of 140 μF are charged during 65ms to a high voltage of +10.5kV (Figure 5a). When the capacitor is fully charged the unit is ready and the big switch can be switched on. Eight outputs of 44kA are connected in parallel and switched simultaneously to provide the 350kA pulse to the Horn.

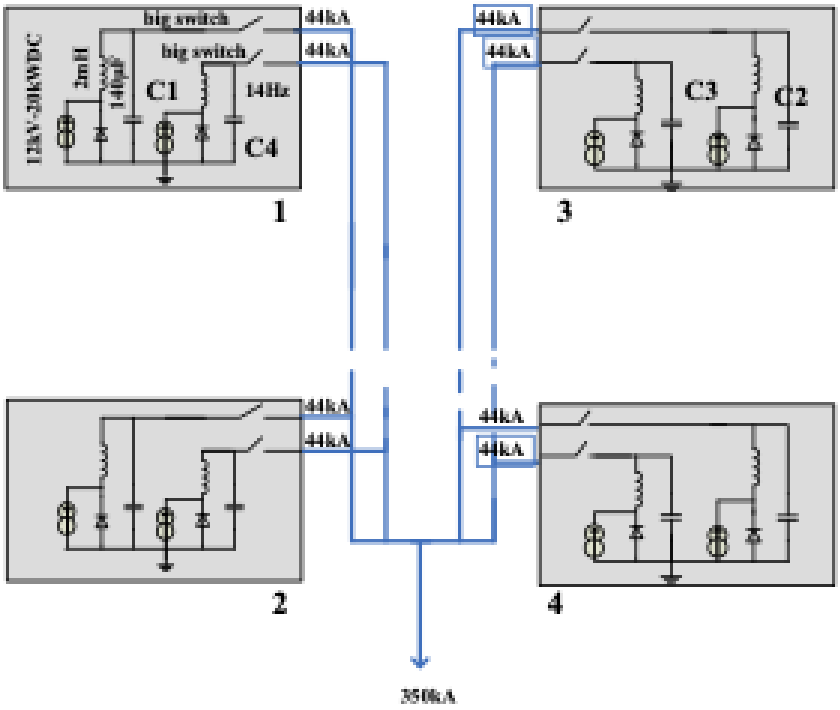


Figure 16: ESSnuSB+ 350kA PSU made by 4 modules of 2X44kA each.

3.1.2 The 44kA output unit

The electrical constraints on an output of 44kA are given in Table 8. Due to the time for recovery the energy, the charger must operate in only 65ms. The low values of electrical resistivity in discharge and recovery circuits, allows to limit the charger current at 4% of the total current used to provide the 44kA pulse. Therefore, we need a current charger that deliver only 19kW of average power and 21kW of peak power at 14Hz.

Table 8: Electrical constraints at $V_c = 10.5\,\mathrm{kV}$ (44 kA output module)

Operating mode	F **[Hz]**	dI/dt **[A/μs]**	I_{PEAK} **[A]**	I_{RMS} **[A]**	Q **[C]**
Charge	14	–	2	1.8 (DC)	0.117
Recovery	14	5.9	2500	270	2.783
Discharge	14	1370	44000	1160	2.9

By connecting the diode Dr in parallel of the output of the charger we also damage of negative voltage on the charger while increasing its reliability.

3.2 Mechanical implantation

A proposition of mechanical implantation of components is shown in sketch of Figure 17. This solution allows to use a minimal ground area implantation of 10 m². The striplines length is reduced to the minimum.

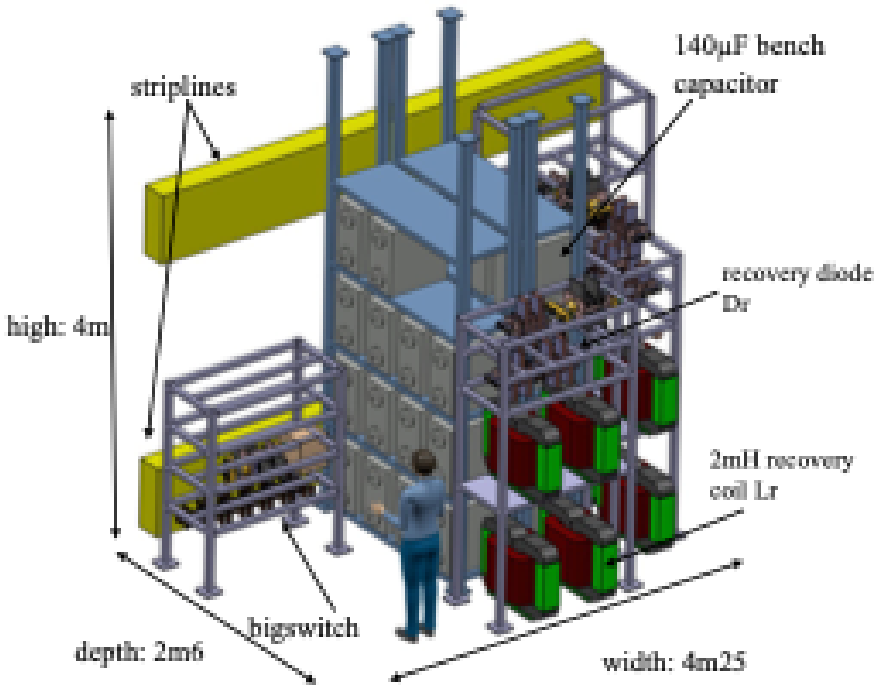


Figure 17: ESSnuSB+ 2X44kA PSU module.

The place occupied by each mains component is given in Table 9. The ground mechanical constraints are $1\,\mathrm{t\,m^{-2}}$ in average and they can attain a maximum of $50\,\mathrm{t\,m^{-2}}$ at the contact between ground and support feet.

Table 9: Update volumes and weights of PSU 1X44kA module components for ESSnuSB+.

Component	**Total dimensions [m]** $(W \times H \times D)$	**Total weight [kg]**
Big switch ARCEL-2x7V0006M ATESYS	$1.35 \times 1.55 \times 0.30$	400
Recovery Diode ARCEL	$(1.40 \times 0.525 \times 0.72) \times 2$	200
Recovery Coil 2 mH 4x7V0005M-ATESYS	$(0.80 \times 0.62 \times 0.40) \times 4$	1600
Bench Capacitor 140 μF 14x26ECF009-AVX	$(0.55 \times 0.57 \times 0.31) \times 14$	1900
Current Charger +10.5 kV 21 kWDC CCR24-TECHNIX	$0.54 \times 0.65 \times 0.30$	50
Three Mechanical Support	–	1300
TOTAL for a 1×44 kA module	–	**5500**

Figure 18 give us an idea of total PSU area implantation with a total area of 320 m^2 and a 4 m minimum height. This area take account area implantation for ESSνSB with 16 modules. The length of striplines (in yellow) from the horns to the last module have been limited to 33 m due the electrical constraints. The preliminary design of the Target Station facility does not take into account others rooms for the maintenance of the electrical modules.

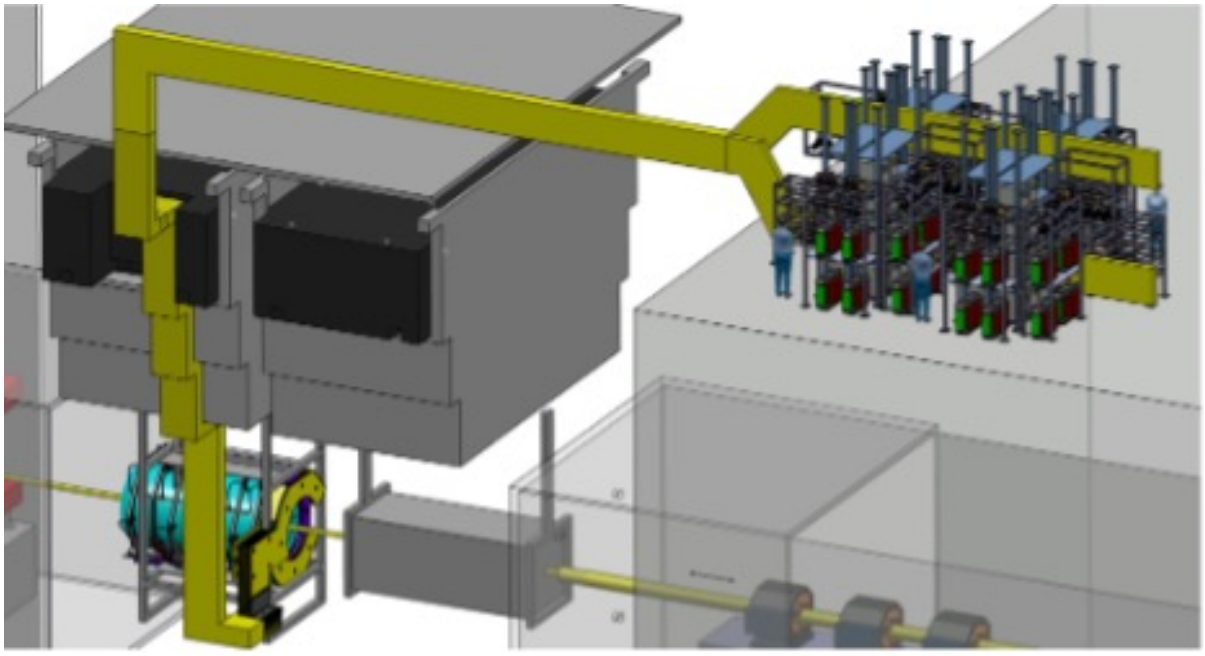


Figure 18: Preliminary 3D layout of the PSU placed on top of the target station and switch yard tunnel

4 The focusing and the pion extraction systems .

The transition region between the magnetic horn and the racetrack ring is called the T2R line. This lines contains several magnetic systems which will select and transport the pions at a specific central momentum 700 MeV/c required for the operation of the LEnuSTORM ring [11]. The first element located downstream of the horn is the LADM allowing to select the pions by applying a uniform magnetic field in the propagation region. The geometry of the LADM requires a large aperture to have enough intensity and has been chosen regarding the width of spatial distribution of the pions at the entrance of the dipole. The previous study showed a good uniformity [12].

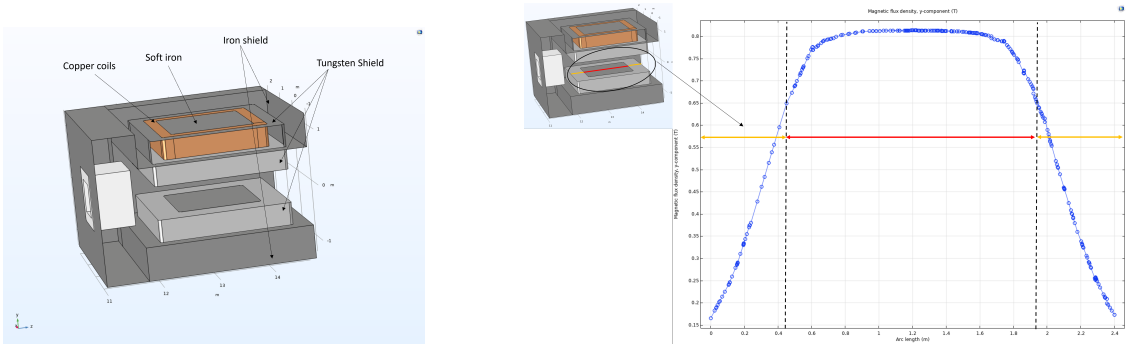


Figure 19: Geometry of the LADM COMSOL Model (Left). By component of the magnetic field at the central trajectory and for y = 0 for B field at y = 0 cm along the pion beam (z-) (Right).

However, the levels of radiations in the aperture region imposed two additional tungsten rings to shield the two coils and the PEEK material used as electrical insulator for the wires. The geometry of the dipole, simulated with COMSOL Multi Physics [13], is shown in Figure 19 (Left) and a magnetic field uniform in Figure 19 (Right). Furthermore it must be robust enough to withstand the radiation levels in the aperture region and for the at the coils levels and will be justify on the next section.

After deviation, the pions enter in the T2R lines whose the concept is shown in Figure 20.

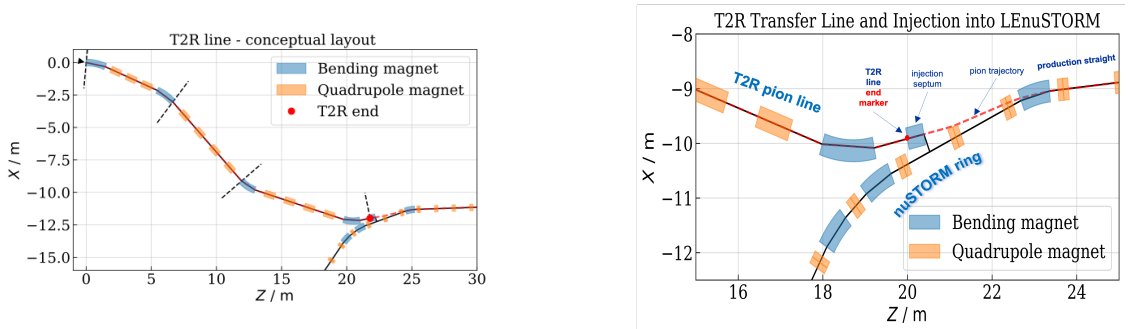


Figure 20: Concept of the Target to Ring (T2R) pion transfer line (Left) Injection into the LEnuSTORM ring. (Right)

The principle has been described in previous documents and shown in Figure 20. The lines consists in three segments, the target station arc designed for matching the pion production from the horn/collimator, the injection-matching arc to match to the parameters of the pion beam in nuSTORM injection point and have zero dispersion at the start of the production straight, and finaly the Dispersion-suppression straight which connect the optics between the two arcs.

5 Target Station Facility

The target station facility in Phase 2 (ESSνSB+) ans Phase 3 (ESSνSB) share the same design concerning the hadronic collector location. Since most the shielding of the building has already been studied for 5 MW beam power it will be considered sufficient for phase 2 in term wall thickness made of concrete and for the iron shielding surrounding the hadronic collector. For this reason, the use of the reduced model will be sufficient to study the downstream part elements in particular the LADM.

5.1 Power deposition and shielding

To protect the experimental area and critical components, in particular the dipole coils, several shielding and protection elements are included in the target station design.

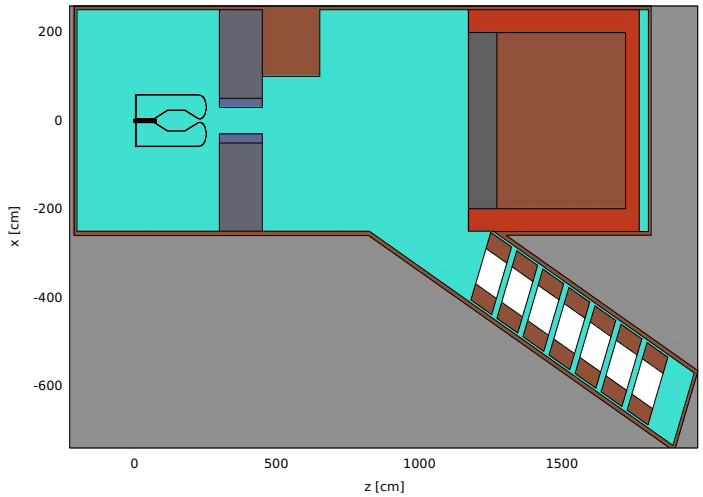


Figure 21: Target Station Facility reduced model.

Figure 21 shows the complete simulation layout. Immediately downstream of the magnetic horn, a collimator is located at $z = 300$ cm and extends up to $z = 450$ cm. Its primary purpose is to absorb a significant fraction of the secondary radiation produced in the target and horn, thereby reducing the radiation load on the downstream components. The bending dipole is located downstream of the collimator and is used to deflect the secondary beam towards the downstream transfer line. At approximately $z = 850$ cm, the transfer line tunnel begins, with several quadrupole magnets used to control and transport the secondary beam. Finally, at $z = 1070$ cm, a beam dump is introduced to absorb the remaining beam and associated secondary radiation, limiting the radiation reaching the downstream part of the facility.

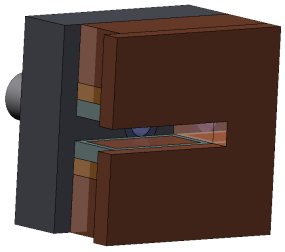


Figure 22: Collimator - Dipole configuration used in the FLUKA simulation.

A more detailed view of the CLMT and dipole system is presented in Fig. 22. The magnetic horn is shown on the left in light grey, followed by the collimator shown in dark grey. In the simulated configuration, the main body of the CLMT is composed of 90% 316LN stainless steel and 10% water. An inner tungsten insert, referred to as the tungsten ring, is included to enhance radiation absorption. It is composed of 85% tungsten, 5% tantalum and 10% water.

Downstream of the CLMT, the dipole magnet is represented with a U-shaped geometry in order to provide a large aperture for the secondary beam while reducing the probability of particles interacting directly with the magnet structure. The yoke is made of iron and the coils are made of copper. Additional tungsten shielding is placed above the coils to reduce radiation and energy deposition in the electrical components of the magnet. This shielding is particularly important because the dipole coils are exposed to secondary particles produced upstream.

An additional Downstream shielding structure (DSS) is included to provide further protection of the dipole against radiation originating from downstream components, including secondary particles generated by interactions in the beam dump.

Finally, the beam dump consists of three main material regions. A graphite block is used as the primary beam-intercepting material, providing a robust medium for absorbing the incoming beam power. It is followed by a large iron block providing additional absorption of the remaining hadronic and electromagnetic shower. These components are surrounded by a CuCr1Zr copper alloy structure, providing efficient heat conduction and dissipation. The CuCr1Zr alloy considered in the simulation consists of 98.9% copper, 1% chromium and 0.1% zirconium.

Overall, the combination of the collimator, local shielding around the dipole, downstream shielding and beam dump is designed to limit radiation transport towards sensitive components and the surrounding experimental area, while allowing efficient transport of the useful secondary pion beam through the target station.

Table 10: Power deposited in the main components of the target station. The deposited power corresponds to the mean value obtained from 140 independent simulations of 75k primary protons each. The standard error is computed as $\sigma/\sqrt{N}$, where σ is the standard deviation across simulations and $N = 70$ is the number of simulations.

Component	**Deposited Power [kW]**	**Standard Error [W]**
Target	124	19
Horn	34.4	12
Fe Shielding	294	87
W Shielding	160	80
Fe Dipole	9	17
Cu Dipole	0.15	0.7
W Dipole	4.20	1.1
DS Shielding	3.81	10
Cu Beam Dump	8.22	15
Fe Beam Dump	82.4	55
C Beam Dump	148	82
Vessel	123	35
Walls	58	21

Table 10 shows the power deposition in the different components of the simulation. As expected, the target and shielding components receive the highest power deposition, with more than 100 kW deposited in these regions. In contrast, the dipole coils are among the most protected components, with a power deposition of only 0.15 kW.

The power deposition was also monitored throughout the simulation. Figure 23 shows a projection of the energy deposition across the simulated geometry, illustrating the proton beam impact location and the regions receiving the highest radiation loads. This figure complements the results presented in Table 10.

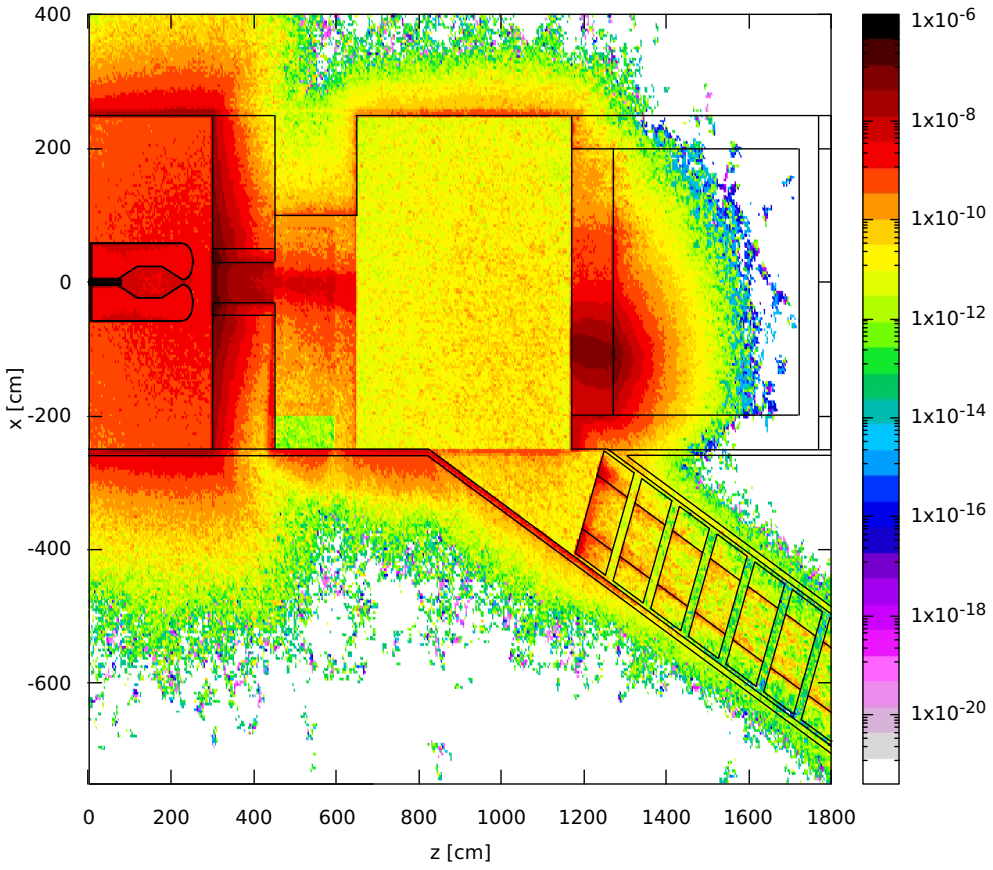


Figure 23: Energy distribution across the FLUKA simulation. The colorbar represents the energy [GeV/cm^3] deposited in each voxel, averaged over the whole y axis.

Most of the energy is deposited upstream of and within the CLMT, while downstream of the CLMT, the beam dump accounts for the largest share of the energy deposition. However, the tungsten shielding and iron yoke of the dipole also absorb several kilowatts, with power depositions of 4.20 kW and 9 kW, respectively.

5.2 Dose deposition at the dipole level

Regarding the dose received by the dipole coils, a dedicated study was performed to significantly reduce the radiation dose level within the coils. Figure 24 shows the temporal evolution of the dose received by the coils for different tungsten shielding thicknesses.

The initial simulations considered a geometry without tungsten shielding, resulting in a relatively short expected lifetime of the coils and a large dispersion in the maximum local dose. The addition of tungsten significantly reduces both the overall dose received by the coils and the dispersion of the dose distribution. The geometry adopted in the current design includes a 40 cm-thick tungsten shielding layer, which is expected to allow more than 10 operational years under the considered irradiation conditions.

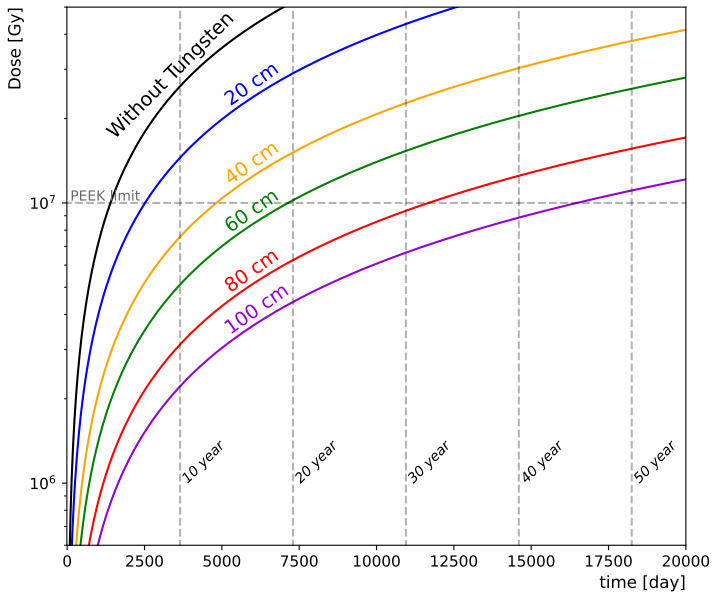


Figure 24: Dose evolution in the dipole coils over time. One year corresponds to 365 operating days. Each curve represents the dose evolution for a given tungsten plate thickness.

Several limitations should nevertheless be considered when interpreting these results. First, one operational year is defined here as 365 operating days. Second, the reported dose corresponds to the prompt dose only. Furthermore, the dose shown in Fig. 24 is an averaged value over the coil region. The maximum local dose should therefore also be considered when assessing the lifetime of the coils. For the 40 cm tungsten configuration, the maximum local dose reaches approximately 5.67×10^7 Gy after 10 operational years. This value is approximately ten times higher than the average dose, whereas the corresponding ratio was around 150 for the configuration without tungsten shielding.

Consequently, although the average dose suggests a lifetime exceeding 10 operational years, localised regions of the coils may reach significantly higher dose levels and could potentially fail earlier. A more detailed assessment of the spatial distribution of the dose within the coils, together with an evaluation of the corresponding material damage and lifetime limits, should therefore be performed in future studies.

6 Conclusion

In this deliverable, the main elements of the target station of the ESSνSB+ have been summarized, which will feed in pions the Low Energy neutrinos from STOred Muons (LEnuSTORM) ring with a 1.25 MW proton beam delivered by an upgraded of the ESS. The proposed project is in coherence with the schedule of the power evolution of the ESS projet.

The ESSνSB horn shape has been re-optimized for the ESSνSB+ project using the similar deep learning technique based on a genetic algorithm to maximize the pion yield in the LEnuSTORM ring. At this level, some possibilities remains open for further optimisation taking in account for instance a more complete parametrisation of full line.

The simulation of the packed bed target with pressurized helium has been performed and reveals additional improvement regarding the mechanical structure deformation with the high power deposition in the medium. In addition, some measurements have been done thanks to the ETTF facility based at ESS using a reduced granular target.

The proposed scheme for the power supply unit follows a similar approach compared to the previous project and has been updated regarding the new electrical parametrisation of the horn with respect to the ESSνSB+ conditions.

New elements has been proposed like the Large Aperture Magnet Dipole which is a key element in the ESSνSB+ project to select the pions and send them in the race track ring thanks to the Target to Transfer line. Additional shielding has been proposed to protect the sensitive part of the LADM like the coils.

The ESSνSB+ target station facility is similar to the design of the ESSνSB except the 50 m long decay tunnel. The shielding defined in phase 3 can be safely considered in phase 2.

References

[1] A. Alekou et al. The European Spallation Source neutrino super-beam conceptual design report. *Eur. Phys. J. ST*, 231(21):3779–3955, 2022. [Erratum: Eur.Phys.J.ST 232, 15–16 (2023)].

[2] C. Ahdida et al. New Capabilities of the FLUKA Multi-Purpose Code. *Front. in Phys.*, 9:788253, 2022.

[3] Vasilis Vlachoudis. FLAIR: A powerful but user friendly graphical interface for FLUKA. In *International Conference on Mathematics, Computational Methods & Reactor Physics 2009*, pages 790–800, 2009.

[4] ESS Bilbao. ESSnuSB+ Target: First Annual Meeting. Technical report, ESS Bilbao, October 2023. Internal WP3 presentation, 16 October 2023.

[5] ESS Bilbao. Passive Flow Diversion Thermomechanical Study. Technical Report ESSB-ESSNU-ETTF-TP-001, Revision 0.0, ESS Bilbao, October 2026.

[6] ESS Bilbao. ESSnuSB+ Target Update: Passive Flow Diversion Study. Technical report, ESS Bilbao, July 2026. Internal WP3 presentation, slides dated 8 July 2026.

[7] ESS Bilbao. ESSnuSB+ WP3 Target: Fourth Annual Meeting. Technical report, ESS Bilbao, October 2026. Internal WP3 presentation, 6 October 2026.

[8] ESS Bilbao. Target–horn integration: external-HTC sweep and slot-bypass structural assessment. Internal CFD and Mechanical calculation records, October 2026. Calculations and temperature-transfer verification, 28–29 October 2026.

[9] Volker Gnielinski. Heat transfer coefficients for turbulent flow in concentric annular ducts. *Heat Transfer Engineering*, pages 431–436, 2010.

[10] Siemens Digital Industries Software. Simcenter PSIM: Power Electronics Simulation Software. https://www.siemens.com/en-us/products/simcenter/systems-simulation/psim/, 2026.

[11] MS6 : Evaluation of the LEnuSTORM requirements and parameter range, 2024.

[12] ESSnuSB+ WP3. D3.2, preliminary design of the pion extraction and focusing system, 2025.

[13] COMSOL Multiphysics® v. 5.4., 2024.